Long-range superconducting proximity effect in nickel nanowires

Jue Jiang,[1] Weiwei Zhao,[1] Fei Wang,[1] Renzhong Du,[1] Ludi Miao,[1] Ke Wang,[2] Qi Li,[1]
Cui-Zu Chang [1] and Moses H. W. Chan [1,*]

[1]*Department of Physics, The Pennsylvania State University, University Park, Pennsylvania 16802, USA*
[2]*Materials Research Institute, The Pennsylvania State University, University Park, Pennsylvania 16802, USA*

When a ferromagnet is placed in contact with a superconductor owing to incompatible spin order, the Cooper pairs from the superconductor cannot survive more than 1 or 2 nm inside the ferromagnet. This is confirmed in the measurements of ferromagnetic nickel (Ni) nanowires contacted by superconducting niobium (Nb) leads. However, when a 3 nm thick copper oxide (CuO) buffer layer made by exposing an evaporated or a sputtered 3 nm Cu film to air is inserted between the Nb electrodes and the Ni wire, the spatial extent of the superconducting proximity range is dramatically increased from 2 to a few tens of nanometers. A scanning transmission electron microscope study confirms the formation of a 3 nm thick CuO layer when an evaporated Cu film is exposed to air. Magnetization measurements of such a 3 nm CuO film on a SiO_2/Si substrate and on $Nb/SiO_2/Si$ show clear evidence of ferromagnetism. One way to understand the long-range proximity effect in the Ni nanowire is that the CuO buffer layer with ferromagnetism facilitates the conversion of singlet superconductivity in Nb into triplet supercurrent along the Ni nanowires.

I. INTRODUCTION

The leakage of Cooper pairs extends superconducting behavior into a normal metal when it is placed in direct contact with a superconductor. The spatial range of such a proximity effect can be as long as 1 μm [1,2]. However, when the normal metal is replaced by a ferromagnet, the proximity-induced superconductivity is expected to decay rapidly inside the ferromagnet and vanish within 1 or 2 nm due to the incompatible nature of superconductivity and ferromagnetic order [2]. This expectation was confirmed in macroscopic (Fe, Ni)-In junctions [3] and submicron Ni-Al structures [4] where the spatial range of the proximity effect is found to be $\sim$1 nm. On the other hand, a surprisingly long-range proximity effect was found in a number of experiments on mesoscopic superconductor-ferromagnet (SF) hybrid structures [5–12]. Supercurrent was detected in a half-metallic ferromagnet CrO_2 thin film sandwiched between two singlet superconducting electrodes separated by 1 μm [10,13]. To account for the unusually long-range proximity effect, the induced superconductivity in the CrO_2 film was attributed to spin-triplet pairing instead of the usual singlet state. Josephson junctions with tailored magnetic profiles were fabricated to test this spin-triplet generation mechanism, where the ferromagnetic Co layer is sandwiched between two conical

magnetic Holmium (Ho) layers of 4.5 and 10 nm thickness [7], whose magnetic moments follow a helical pattern along the c axis at low temperatures. It displayed a relatively constant voltage, which is the critical current multiple normal-state resistance (I_cR_N), as a function of the thickness when the ferromagnetic Co layer is up to 16 nm. In the absence of the Ho layers, I_cR_N would decrease exponentially. Similar results [8,9] have been found when a weak ferromagnetic layer PdNi (2.8 nm) or CuNi (1.4 nm) was inserted as buffer layers between Nb and Co/Ru/Co. In these systems, I_cR_N remains constant when the Co layer is increased to 28 nm, indicating the robustness of spin-triplet superconductivity against the presence of a ferromagnet. Similar spin-triplet-induced long-range superconductivity recently observed in the Josephson junction consists of a newly discovered triangular magnet, $K_{1-x}V_3Sb_5$ [14].

A long-range proximity effect was also reported in ordinary hard ferromagnetic Co and Ni nanowires (NWs) contacted with superconducting tungsten (W) electrodes [15]. The nanowires were grown electrochemically inside a porous membrane and "harvested" individually for measurements. The electrodes, containing approximately 40% atomic carbon and 20% atomic gallium were deposited onto the NWs by the focused ion beam (FIB) technique and have a superconducting transition temperature T_c of $\sim$4.5 K, well above that of pure W at $T \sim 12$ mK. The key findings, measured with a four-probe configuration, are that a Co NW of 40 nm diameter was driven completely superconducting with zero resistance when sandwiched between two superconducting W voltage electrodes separated by 600 nm. For longer Co NWs of 40 and 80 nm diameter and 1.5 μm length and Ni NWs of 60 nm diameter and 3 μm long, the residual resistances found after the superconducting drop in the low-temperature limit

were 11%, 50%, and 52%, respectively, of the normal state resistance. The long-range proximity effect is also seen in a configuration where a superconducting W strip is placed in contact with the Co NW but is not part of the measurement circuit. The deposition of the W electrodes onto the NWs by the FIB deposition process involves the bombardment of high-energy ions of the NW. This process very likely produces defects and inhomogeneous magnetic moments in W/Co and W/Ni contact regions. It was proposed that [10,16–18] the conversion from singlet to triplet superconductivity requires inhomogeneous magnetic moments. It is reasonable to interpret the long-range proximity effect in Co and Ni NWs to be a consequence of triplet superconductivity induced by the inhomogeneous magnetic moment at the W/Co and W/Ni contact regions. The results of Ref. [15] were later replicated by another group [19]. The major drawback of these two experiments is that the deposition of the W electrodes by FIB is not a well-controlled process. The experimental studies [5–15,19] cited above generated considerable excitement in the condensed matter community since spin-triplet superconductivity, including that generated by the proximity effect, is thought to host topological excitations that may be utilized for quantum computations [17].

Here we report an experiment that shows the spatial extent of the proximity effect along a Ni NW is dramatically lengthened by nearly two orders of magnitude upon the insertion of a 3 nm thick naturally oxidized thin Cu buffer layer between the superconducting Nb electrodes and the NW. In contrast, the insertion of an Au buffer layer or 3 nm Cu buffer layer prevented from oxidizing gives rise to a much smaller superconducting proximity range. Additionally, the insertion of 10 nm thick Cu with and without natural oxidation shows no enhancement in the proximity distance. Magnetometry measurements on these different Cu films indicate that only the 3 nm thick oxidized Cu buffer layer exhibits ferromagnetic properties.

II. METHODS

In our experiment, samples were fabricated by *e*-beam lithography followed by physical vapor deposition (PVD). Materials with different functionalities were deposited separately to assure comparatively clean interfaces with minimal intermixing. The superconducting Nb electrodes [500 nm (wide)×40 nm (thick)] in all samples were made by dc magnetron sputtering on the Si/SiO$_2$ substrates. Consistent superconducting transition temperature (T_c) is found near 8 K. The background vacuum of the sputtering process is $\sim 5 \times 10^{-7}$ mbar, and argon pressure is 4×10^{-3} mbar for exciting the plasma. The deposition of the ferromagnetic Ni or Cu buffer layer is carried out either by sputtering or thermal evaporation with a background vacuum of $\sim 1 \times 10^{-6}$ mbar. These PVD-made NWs typically have a polycrystalline structure [20]. The schematic and optical images for a typical transport measurement circuit are shown in the inset of Fig. 1(a). Low-temperature transport measurements are carried out in the physical property measurement system (PPMS) and its auxiliary dilution fridge inserts from Quantum Design.

III. EXPERIMENTAL RESULTS

Figure 1(a) shows four-probe magnetotransport measurements of sample 1, a Ni NW [400 nm (wide) × 40 nm (thick)] deposited by thermal evaporation, followed by exposure to air during a second nanofabrication step prior to the sputtering of superconducting Nb electrodes [500 nm (wide) × 40 nm (thick)] on top of the oxidized Ni NW. The observed small drops in resistance at low temperature [Fig. 1(a)] and low magnetic field [Fig. 1(b)] are signatures of superconductivity in the magnetic Ni nanowire in contact with the superconducting Nb voltage leads. Since the total length of the Ni NW between the voltage leads is 500 nm and the total drop in resistance seen under zero magnetic field is ∼0.9% at $T \sim 0.5$ K, the spatial range of the proximity effect in the Ni NW is estimated to be ∼2 nm, in good agreement with theoretical expectations [1,2]. Figure 1(b) also shows, as expected, that the proximity-induced resistance drop decreases with the application of an out-of-plane external magnetic field and elevated temperature. R-$\mu_0 H$ relations at $T \sim 8$ K indicate an anisotropic magnetoresistance (AMR) on top of the superconducting resistance drop, giving rise to a "step" feature in magnetoresistance upon reversing the direction of the magnetic field. This resistance difference due to AMR does not exceed ∼0.4% of average resistance. The inset in Fig. 1(b) shows the two-terminal resistance measurement under zero magnetic field. The large two-terminal resistance (3.4 kΩ above 8 K and nearly 2 kΩ below 4 K) and the substantial scatters in the four-terminal resistance value indicates there is an insulating Ni oxide layer between the Nb electrodes and the Ni NW. The drop in two-terminal resistance near 8 K pinpoints the superconducting transition of at least one of the Nb electrodes at this temperature. The additional resistance drop seen near 4 K may locate the T_c of other Nb electrodes. In addition, the inset of Fig. 1(b) shows an upturn in the two-terminal resistance value below 2 K; this upturn is very likely the signature of Mott insulator behavior of the Ni oxide layer.

In Figs. 1(c) and 1(d), we present transport results of sample 2 which shows a very small two-terminal resistance (305 Ω above and 20 Ω below 8K). For this sample, a 3 nm thick Au layer was evaporated onto the NWs prior to sputtering the Nb electrodes. Both R-T and R-$\mu_0 H$ scans show "critical peaks" near the superconducting transition of the Nb electrode. These peaks have been reported in prior studies [13–15,21,22] but the physical origin of these peaks is not yet clear. Below the superconducting transition of the Nb leads, the resistance of the Ni NW drops rapidly by ∼4% and flattens out quickly with decreasing T and external magnetic field. The 4% drop translates to a superconducting proximity range of ∼10 nm, indicating that the insertion of the Au buffer layer, while improving very significantly the contact transparency between Nb leads and the Ni NW, the enhancement of the spatial range of the proximity effect is modest. In another sample, we evaporated a 6 nm Au film over the entire length of the Ni NW before sputtering Nb leads (sample 8, Supplemental Material, Fig. S4 [23]). This sample exhibits a nearly identical proximity range of 10 nm. This result suggests the ferromagnetism of the Ni NW prevented the thin Au layer along its entire length from being driven to be superconducting by the Nb leads [24,25].
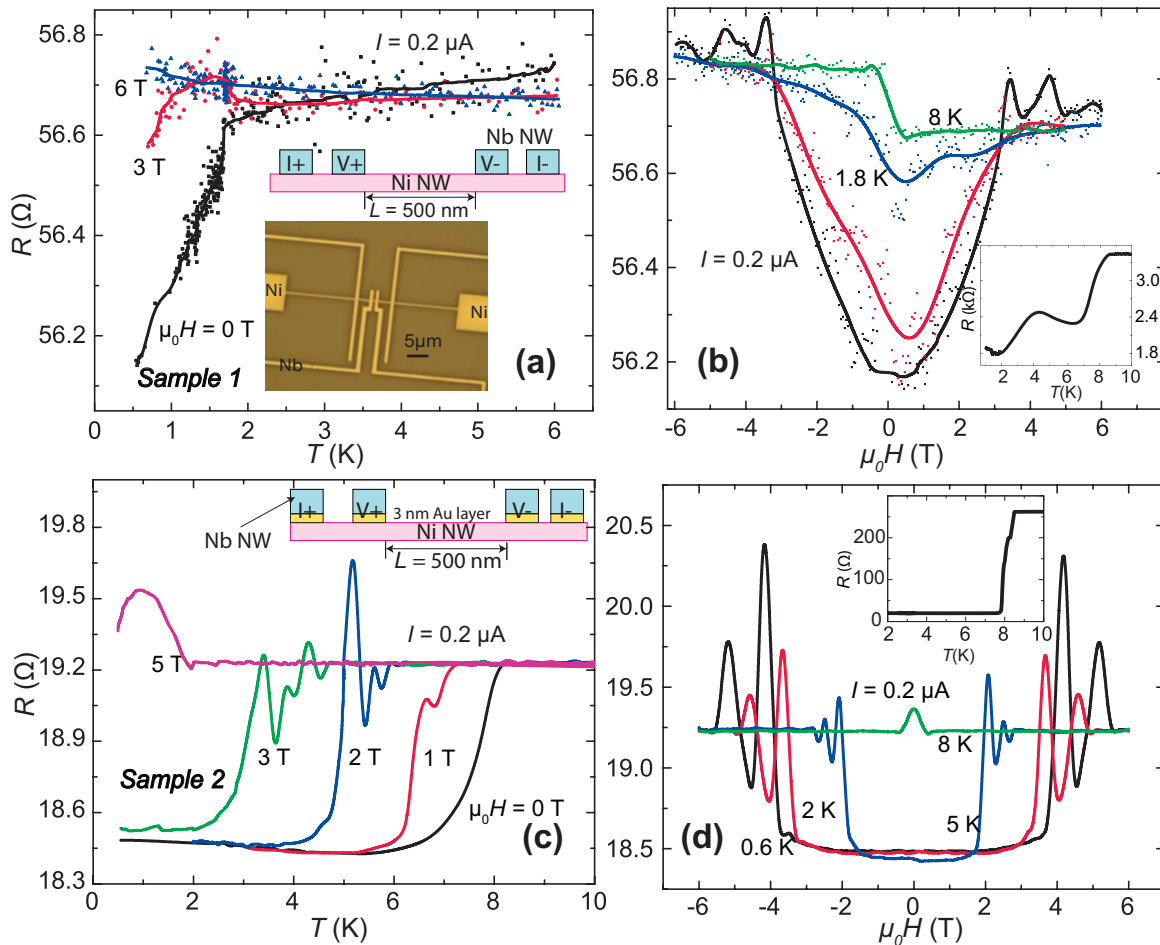
FIG. 1. R-T and R-$\mu_0 H$ curves of Ni nanowires contacted by superconducting Nb electrodes without or with an Au buffer layer. (a) In sample 1, a Ni NW (pink) was thermally evaporated on the SiO_2/Si substrate and then exposed to air and moved to a different chamber for sputtering of tNb electrodes (blue). At zero magnetic field, the resistance R starts to drop at $T \sim 1.5$ K. Since the drop at $T \sim 0.5$ K is $\sim 0.8\%$ of the resistance of the normal state, the superconducting proximity range is ~ 2 nm. Inset: a schematic drawing and an optical image of sample 1. (b) R-$\mu_0 H$ curves of sample 1 under different temperatures. Inset: The two-terminal resistance shows two drops at $T \sim 8$ K and $T \sim 4$ K, possibly indicating different T_c of the two Nb electrodes. An upturn due to the Mott insulator behavior of Ni oxide is found below 2 K. In (a,b), the dots are the raw data and the lines are guides for the eye. (c) In sample 2, the Ni NW (pink) was thermally evaporated; then it was exposed to air, followed by the second-step lithography and Au (yellow) evaporation. It was taken out of the vacuum and placed in a sputtering chamber for Nb (blue) deposition. At zero magnetic field, the resistance R drop of $\sim 4\%$ corresponds to a superconducting proximity range of ~ 10 nm, indicating a slight enhancement in the spatial range of supercurrent in a Ni NW with an Au buffer layer. (d) R-$\mu_0 H$ curves of sample 2 under different temperatures. Inset: The two-terminal resistance of sample 2. Both R-T and R-$\mu_0 H$ relations show several critical peaks near the superconducting transition regimes, consistent with our prior report [15]. The fabrication details of samples 1 and 2 are listed in Table I. The Ni NW used here is 400 nm wide and 40 nm thick, while the Nb electrodes are 500 nm wide and 40 nm thick.

Figure 2 shows magnetotransport measurements of two different Ni NW samples contacted with Nb leads through a thin CuO buffer layer. In sample 3, the Ni NW was thermally evaporated onto the Si/SiO_2 substrate; it was then taken out of the vacuum for the second lithography step to prepare for the 3 nm Cu film evaporation. The sample was exposed to air again to oxidize the Cu film and was finally placed in the sputtering chamber where Nb leads were attached. For sample 4, Nb electrodes and the 3 nm Cu film were sputtered sequentially without breaking vacuum; then the sample was taken out from the vacuum and went through the second lithography step for Ni NW sputtering. Since the Cu films in both samples were exposed to air for a few hours, there

is inevitably a CuO layer between the Nb electrodes and the Ni NWs in both samples. Our scanning transmission electron microscopy and energy-dispersive x-ray spectroscopy studies, presented below, indicate a Cu layer of 3 nm thickness similarly exposed to air is likely to be oxidized. Since the Nb and Cu films of sample 4 were sputtered sequentially without breaking the vacuum, there may be an oxide-free Nb/Cu interface between the Nb electrode and the CuO buffer layer in sample 4.

Since the voltage leads of sample 3 are separated by a distance L of 500 nm the resistance drop of 30% from 3 to 0.2 K, indicates a superconducting proximity spatial range of 65 nm. This means the insertion of a 3 nm CuO layer between the
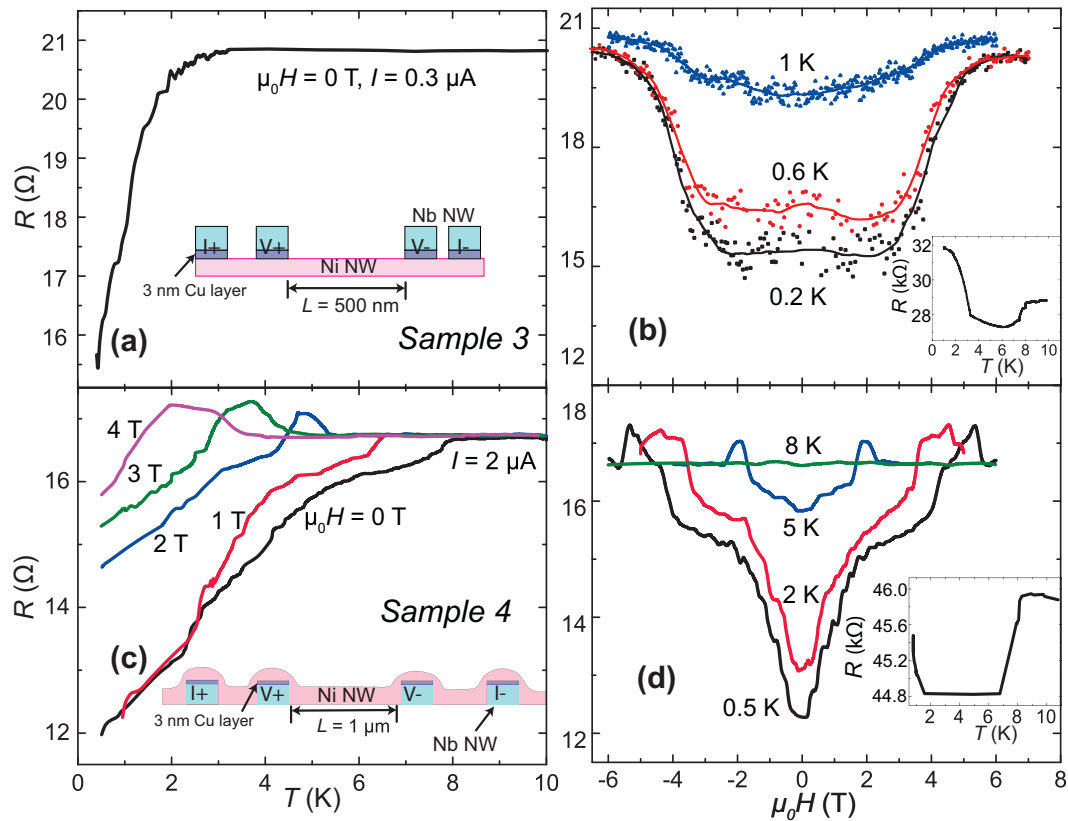
FIG. 2. R-T and R-$\mu_0 H$ curves of Ni nanowires contacted by Nb electrodes with 3 nm CuO buffer layers. (a) In sample 3, a Ni NW (pink) was thermally evaporated, then it was taken out of the vacuum for the second-step lithography and the Cu film (purple) evaporation, and then it was exposed to air again before being placed in a sputtering chamber for Nb (blue) deposition. The resistance R starts to drop at $T \sim 3$ K and shows a 25% decrease at $T \sim 0.2$ K. This suggests a superconducting proximity range of 65 nm in the Ni NW. Inset: A schematic drawing of sample 3. (b) R-$\mu_0 H$ curves of sample 3 under different temperatures. The dots are the raw data and the lines are the guides for the eye. Inset: The two-terminal resistance of sample 3. A resistive upturn shows up below 3 K due to the Mott insulator behavior of the CuO buffer layer. (c) In sample 4, Nb electrodes (blue) along with the Cu (purple) film were sputtered without breaking vacuum; then it was exposed to air and went through the second-step lithography and Ni (pink) NW sputtering. R-T curves show a superconductivity proximity range of $\sim$136 nm at zero magnetic field. Inset: A schematic of sample 4. (d) R-$\mu_0 H$ curves of sample 4 at different temperatures. Inset: The two-terminal resistance of sample 4; a low-temperature upturn just like sample 3 is found. The fabrication details of samples 3 and 4 are listed in Table I. The Ni NW used here is 400 nm wide and 40 nm thick, while the Nb electrodes are 500 nm wide and 40 nm thick.

Ni NW and the Nb electrode increases the spatial proximity effect by a factor of 30. The magnitude of the resistance drop and the "critical" field value of the phenomenon shows the expected temperature dependence [Fig. 2(b)]. The two-terminal results in the inset of Fig. 2(b) show a drop near 8 K due to the superconducting transition of Nb electrodes. Two-terminal resistance values of samples 3 and 4, near 30 and 45 kΩ, respectively, like that in sample 1, are also much higher than that of the four-terminal values. For samples 3 and 4 the two terminal values, which include the resistances of the 3 nm insulating CuO buffer layers sandwiched between the Ni NW and the two Nb electrodes, show prominent upturn below 3 K (sample 3) and 2 K (sample 4). These upturns as noted above are low-temperature signatures of Mott insulator behavior of the CuO buffer layers. The two-terminal resistance values of these two samples are much higher than that of sample 1 because the thickness of the 3 nm CuO buffer layers is much thicker than that of the nickel oxide layer between the Nb electrodes and the Ni NW in sample 1.

Figures 2(c) and 2(d) show magnetotransport results of sample 4. In contrast to samples 1 and 3, the resistance of sample 4 begins to drop promptly at $T \sim 8$ K, i.e., T_c of Nb, instead of at a lower temperature. The magnitude of the resistance drop of sample 4 indicates a proximity range of 136 nm. In addition, a much larger current than that used in sample 3 is required to completely quench the proximity-induced superconductivity (see Supplemental Fig. S1 [23]). The longer superconducting proximity range in sample 4 is likely due to the aforementioned oxide-free Nb/Cu interface that is more favorable for Andreev reflection. Critical peaks near T_c and H_c as well as a repeatable quasiperiodic oscillation superimposed on background magnetoresistance are observed in sample 4. These oscillations are likely due to the crossing of vortices in the proximity-induced superconducting region [26].

The long superconducting proximity range shows, interestingly, a very significant decrease when we prevent air exposure or increase the thickness of the Cu buffer layer. In sample 5, we first sputtered the Ni NW, and then broke

TABLE I. Summary of the eight samples in the superconductivity proximity studies.

Sample	L (nm)	Fabrication process	Cu oxide	Proximity range along Ni NW (nm)
1	500	Evaporate Ni $\rightarrow$ air/lithography $\rightarrow$ sputter Nb	No	2
2	500	Evaporate Ni $\rightarrow$ air/lithography $\rightarrow$ evaporate 3 nm Au $\rightarrow$ air $\rightarrow$ sputter Nb	No	10
3	500	Evaporate Ni $\rightarrow$ air/lithography $\rightarrow$ evaporate 3 nm Cu $\rightarrow$ air $\rightarrow$ sputter Nb	Yes	65
4	1000	Sputter Nb $\rightarrow$ sputter 3 nm Cu $\rightarrow$ air/lithography $\rightarrow$ evaporate Ni	Yes	136
5	500	Sputter Ni $\rightarrow$ air/lithography $\rightarrow$ sputter 3 nm Cu $\rightarrow$ sputter Nb	Minimal	13
6	500	Sputter Ni $\rightarrow$ air/lithography $\rightarrow$ sputter 10 nm Cu $\rightarrow$ sputter Nb	Minimal	2
7	500	Sputter Nb $\rightarrow$ air $\rightarrow$ sputter 10 nm Cu $\rightarrow$ air/lithography $\rightarrow$ sputter Ni	Yes	<1
8	1000	Evaporate Ni $\rightarrow$ air $\rightarrow$ evaporate 6 nm Au along the entire Ni NW $\rightarrow$ air/lithography $\rightarrow$ sputter Nb	No	10

the vacuum for the second lithography step to prepare for sequential sputtering of Cu (3 nm) and Nb film in the same vacuum chamber without further breaking the vacuum. Such a process eliminated the exposure of the Cu layer to the ambient atmosphere. We saw a superconducting proximity range of only 13 nm at 2 K (see Supplemental Fig. S2 [23]). We repeated the process used for sample 5 to fabricate sample 6 but increased the Cu thickness to 10 nm, resulting in a proximity range of only 2 nm. For sample 7, we purposely exposed the 10 nm Cu buffer layer to air prior to the deposition of Nb, and still found a proximity range of less than 1 nm. We have summarized the preparation procedures of all the NW samples presented in this Letter in Table I for easy reference.

The results we have presented indicate the long proximity range is related to the oxidation of the thin, $\sim$3 nm thick Cu buffer layer in the fabrication process. In contrast to Cu oxide, the Ni oxide layer found at the Ni/Nb interface in sample 1 does not lengthen the proximity range. Interestingly, when the Cu buffer layer between Nb and Ni is increased to 10 nm, either allowed to be oxidized, as in the case for sample 7, or prevented from oxidizing as in the case for sample 6, the proximity remains to be short range at 2 nm.

The existence of the CuO layer is clearly revealed by high-angle annular dark-field scanning transmission electron microscopy (HAADF STEM) and energy-dispersive x-ray spectroscopy (EDS) studies. The specimen is made by evaporating a 12 nm Cu film onto a Si substrate, followed by air exposure for more than 8 h. It was then transferred to the sputtering chamber for Nb deposition. Figures 3(a) and 3(b) show a Nb layer, along with the Cu buffer layer highlighted by the yellow dashed box. Since heavier elements are brighter in the HAADF STEM images, the "dark" layer below the Nb layer represents the oxidized Cu. This Cu oxide layer is more clearly revealed by EDS elemental mapping in Fig. 3(c), where oxygen is found extending between 3 and 4 nm into the 12 nm Cu film. Therefore, the 3 nm Cu buffer layers in our NW samples (namely, samples 3 and 4) that reveal a long-range proximity effects are very likely to be fully oxidized and the 10 nm Cu film in sample 7 is only partially oxidized during air exposure.

To correlate the transport results with magnetic properties of the Cu buffer layer, we grew naturally oxidized 3 nm Cu

film, 3 nm Cu film prevented from oxidizing, and naturally oxidized 10 nm Cu film onto 4 mm $\times$ 4 mm SiO$_2$ (500 nm)/Si (500 μm) substrates. The protocols of how these film samples are made are shown in Table II. A superconducting quantum interference device (SQUID) based magnetic property measurement system (MPMS, Quantum Design) was used to measure the magnetic properties of these samples with the 4 mm $\times$ 4 mm substrates intact and oriented perpendicular to the magnetic field. We also carried out measurements on identical "pristine" substrates and on substrates sputtered with Nb film. The SiO$_2$/Si substrate, labeled as sample $MH1$, exhibits a signature diamagnetic property with a negative linear magnetic field dependence of magnetization (M) on H [Fig. 4(a)]. We followed the same procedure used in growing the Cu buffer layer in samples 3 and 4 by depositing a 3 nm Cu layer on the SiO$_2$/Si substrate, followed by air exposure for more than 8 h. The M-H plots of this sample (sample $MH2$) at 10 and 50 K are shown in Fig. 4(b). For $|H| > 0.5$ T, the plots of M show negative linear dependence on H, or diamagnetic behavior, just like that found for sample $MH1$, the SiO$_2$/Si substrate. For $|H| < 0.2$ T, the plots show inverted sigmoid deviations with hysteresis in addition to the diamagnetic behavior. To reveal the M-H response of sample $MH2$ in the low-field region, we isolate the diamagnetic contribution of the samples. The diamagnetic contribution is obtained by extrapolating the two branches of the linear and parallel M vs H traces, for $|H| > 0.5$ T, and "translating" them along the x or H axis, without changing the slope to go through the origin. Figure 4(c) shows the M vs H response of sample $MH2$ [Fig. 4(b)] with the diamagnetic contribution subtracted. The sample shows standard hysteretic ferromagnetic behavior with a coercive field of 0.2 T. The magnetization also shows an increase with decreasing temperature, and the saturated magnetization at 10 K is found to be 4.8×10^{-6} emu. Since the ferromagnetism originated from the CuO layer on the SiO$_2$/Si substrate, it would be sensible to scale the magnetization by the surface area of the substrate (4 mm $\times$ 4 mm) instead of the volume of the CuO film. The per unit area of saturation magnetization (M_s) of the CuO film is found to be 3×10^{-5} emu/cm^2. The ferromagnetism of the 3 nm CuO film resembles recent findings on thin VSe$_2$ films. Bulk VSe$_2$ is nonferromagnetic bulk but monolayer VSe$_2$ is weakly
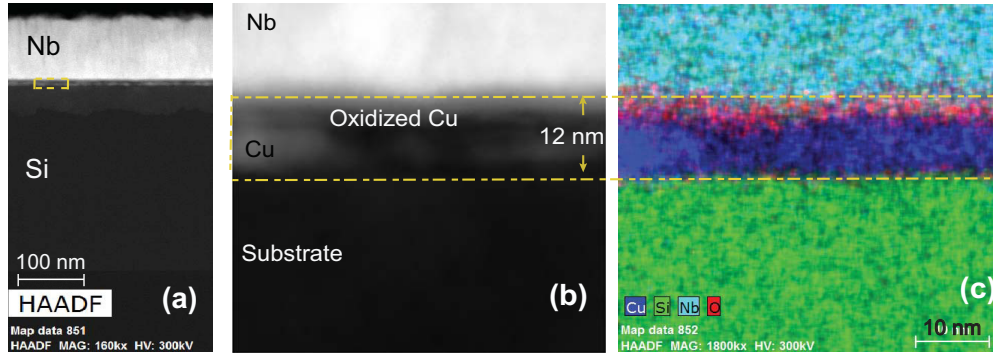
FIG. 3. Cross-sectional STEM images of the partially oxidized Cu film. The Nb film was sputtered after the Cu film was exposed to air. (a) Cross-sectional HAADF STEM image. The yellow dashed box spanning over the Nb, Cu, and SiO$_2$ regions is highlighted and magnified in (b,c). (b) Zoomed-in HAADF STEM image of the magnified region. (c) EDS mappings of the magnified region. It shows an abundance of oxygen, hence CuO, that extends $\sim$3–4 nm into the 12 nm thick Cu film.

ferromagnetic [27,28]. The measured M_s (by area) is found to be 2.4×10^{-4} emu/cm^2 [27], or one order of magnitude larger than the 3 nm CuO film on sample $MH2$.

We note that the *M-H* plots of Fig. 4(c) show only the ferromagnetic behavior without the paramagnetic contribution expected for a magnetic material. The reason for this is that the paramagnetic term scales linearly with H, just like the diamagnetic contribution from the SiO$_2$/Si substrate, with an opposite sign. Since the CuO film is 3 nm thick or 1.5×10^5 times thinner than the 500 μm SiO$_2$/Si substrate, the expected paramagnetic contribution is completely buried by and has been "subtracted" away with the diamagnetic substrate background.

In order to ascertain the finding of ferromagnetic behavior of 3 nm CuO film, we made magnetic measurements on two additional samples prepared with the same procedures as sample $MH2$ (see Supplemental Fig. S3 [23]) [29]. All three samples, samples $MH2$, $MH2$a, and $MH2$b, show similar ferromagnetic behavior. The saturation magnetizations of these samples are, respectively, 3.0×10^{-5}, 2.5×10^{-5} and 1.25×10^{-5} emu/cm^2. The variations reflect the uncontrolled oxidation process of the Cu films. We have also made measurements on a 3 nm oxidized Cu layer deposited on top of the 40 nm Nb layer (sample MHS2 in Supplemental Fig. S3) [23]. Similar ferromagnetic behavior is found indicating the ferromagnetism is not affected by the Nb layer. On the other hand, Fig. 4(d) shows that there is no evidence of any ferromagnetic response in sample $MH3$, a thicker 10 nm Cu

layer that is partially oxidized as demonstrated by the STEM image. Similarly, a 3 nm Cu film sputtered onto Nb layers without breaking vacuum (sample MHS3 in Supplemental Fig. S3) [23], also shows no ferromagnetic response.

IV. DISCUSSION

The magnetization results shown in Figs. 4 and S5 [23] show direct correlation between long-range proximity effect [samples 3 and 4 in Figs. 2(a) and 2(c)] and the ferromagnetism of the 3 nm CuO buffer layer [sample $MH2$ in Fig. 4(c)]. For a thicker, not oxidized, or partially oxidized Cu buffer layer, the absence of ferromagnetism (sample $MH3$ in Fig. 4(d), and sample MHS3 in Fig. S5(c) [23]) is correlated with the absence of long-range proximity effect (samples 6 and 7, in Figs. S3(a) and S3(c) [23]). As noted above, in sample 5, the oxidation of the 3 nm Cu film was prevented because the sputtering of the Cu film and the Nb leads occurred sequentially with the same mask without breaking the vacuum. As expected, in a 3 nm thick Cu film prevented from oxidizing (sample MHS3, Fig. S5(c) [23]) no evidence of ferromagnetism was found. However, a modest (13 nm) proximity range was found in sample 5. We think this modest proximity range may be related to the fact that the edges of the Cu buffer layer in sample 5 not covered by the Nb electrodes are oxidized and become ferromagnetic. The Cu film near the edges of sample $MH3$ used for magnetization measurements is also likely to be oxidized and become ferromagnetic. How-

TABLE II. Summary of the magnetic property of the substrates and thin evaporated Cu films.

| Thin film No.	Sample fabrication	Cu oxide	Ferromagnetic response
$MH1$	SiO$_2$ (500 nm)/Si (500 μm)	No	No
$MH2$	SiO$_2$ (500 nm)/Si (500 μm) $\rightarrow$ evaporate/sputter 3	Yes	Yes
$MH2$a, $MH2$b	nm Cu $\rightarrow$ Air		
$MH3$	SiO$_2$ (500 nm)/Si (500 μm) $\rightarrow$ evaporate 10 nm Cu $\rightarrow$ air	Yes, partially	No
MHS1	SiO$_2$ (500 nm)/Si (500 μm) $\rightarrow$ sputter Nb	No	No
MHS2	SiO$_2$ (500 nm)/Si (500 μm) $\rightarrow$ sputter Nb $\rightarrow$ evaporate/sputter 3 nm Cu $\rightarrow$ Air	Yes	Yes
MHS3	SiO$_2$ (500 nm)/Si (500 μm) $\rightarrow$ sputter 3 nm Cu $\rightarrow$ sputter 3 nm Nb	No	No
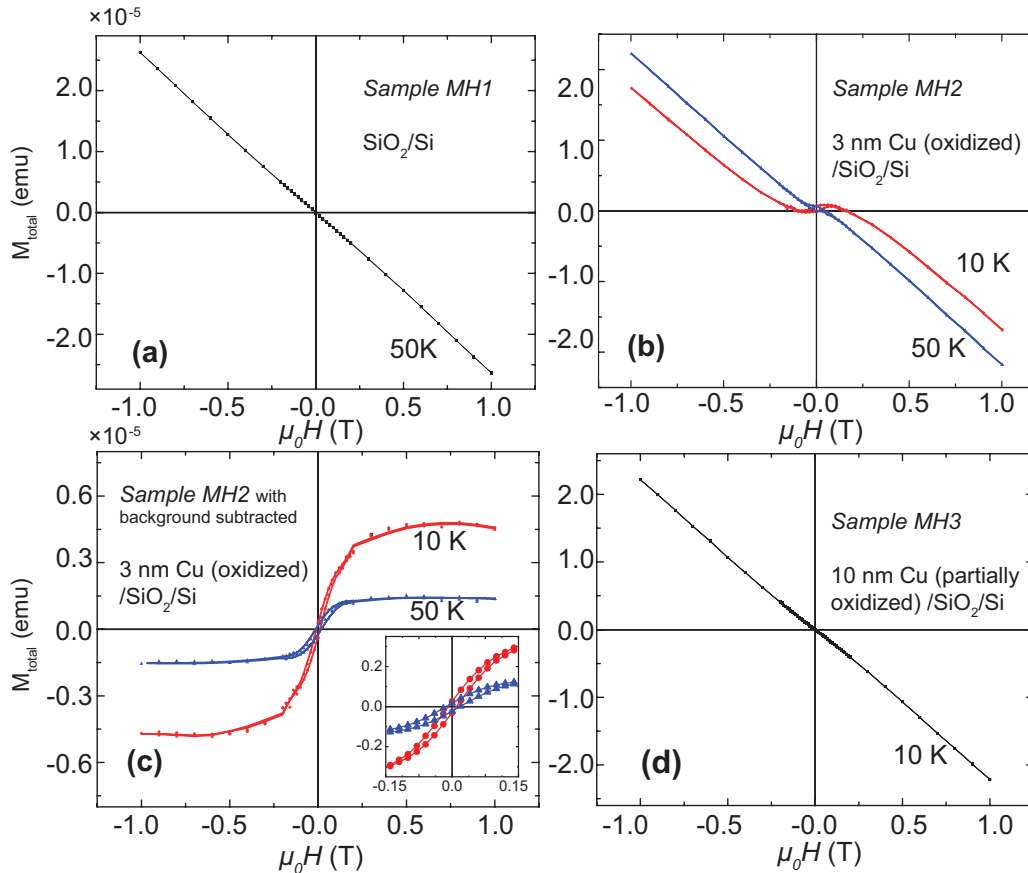
FIG. 4. *M-H* curves of the SiO_2/Si substrate and oxidized Cu films on SiO_2/Si substrate. (a) *M-H* property of a 4 mm × 4 mm SiO_2 (500 nm)/Si (500 μm) substrate (sample *MH*1). The negative linear *M-H* slope demonstrates its diamagnetic property. (b) *M-H* relation of sample *MH*2. The *M-H* curve shows an inverted sigmoid-shape deviation from diamagnetic behavior for μ_0H below 2 kOe. (c) Ferromagnetic response of sample *MH*2 calculated from (b) via procedures explained in the text. Ferromagnetic hysteresis loops are seen at $T \sim 10$ and 50 K. The magnetization increases as the temperature is lowered from 50 to 10 K. Inset: Zoomed-in view of the hysteresis loops. (d) *M-H* relation of sample *MH*3. No ferromagnetic signature is found. The synthesis details of samples *MH*1, *MH*2, and *MH*3 are listed in Table II.

ever, the fraction of the Cu film at the edges compared to that in the interior of the 4 mm × 4 mm sample is minuscule and cannot be picked up by magnetization measurement. The edge to interior fraction of the Cu layer in sample 5 can be many orders larger than that of sample *MH*3. The one-to-one correlation between the ferromagnetism of the fully oxidized Cu buffer layer and the long spatial superconducting proximity effect in the Ni NW demonstrate a causal relationship between these two phenomena.

This ferromagnetic behavior in the naturally oxidized Cu layer of different thickness agrees with the ferromagnetic response reported for nanoparticles or thin-film CuO [30–35]. In CuO nanoparticles, weak ferromagnetism is attributed to uncompensated surface spins. Reference [34] reports the size-dependent magnetic property of CuO nanoparticles. Specifically, it reports that antiferromagnetism is dominant when the diameter (d) is larger than 10 nm, but weak ferromagnetism emerges when d is smaller than 10 nm. References [32,33] show that the oxygen vacancies are a source of the uncompensated spins. Based on Néel's model [36,37], the magnetic moment of a nanostructure depends on the inequality of an antiferromagnet's two antiparallel sublattices,

which are influenced by morphology, crystal structure, and size. When the alternating sublattice "neutral" planes have incomplete top and bottom surfaces, the magnetic moment will be inversely proportional to the dimension of the nanostructure. The ferromagnetism in our 3 nm thick oxidized Cu film appears to share the same physical origin in these CuO nanostructures. As noted above, the ferromagnetism of the 3 nm CuO film resembles that of thin VSe_2 films.

V. CONCLUSIONS

In summary we have presented results that show the thin ferromagnetic oxidized Cu buffer layer is responsible for the possible spin-triplet superconductivity with long proximity spatial range along the length of ferromagnetic Ni NW. Since the deposition and natural oxidation in the ambient atmosphere of a thin, $\sim$3 nm Cu layer between superconducting electrodes and a ferromagnetic NW is a simple and easily reproducible process, the results presented here open an easily accessible procedure for generating spin-triplet superconductivity for systematic in-depth studies.

[1] R. B. Vandover, A. Delozanne, and M. R. Beasley, J. Appl. Phys. **52**, 7327 (1981).

[2] P. G. Degennes, Rev. Mod. Phys. **36**, 225 (1964).

[3] A. I. Buzdin, Rev. Mod. Phys. **77**, 935 (2005).

[4] Y. N. Chiang, O. G. Shevchenko, and R. N. Kolenov, Low Temp. Phys. **33**, 314 (2007).

[5] R. S. Keizer, S. T. B. Goennenwein, T. M. Klapwijk, G. X. Miao, G. Xiao, and A. Gupta, Nature (London) **439**, 825 (2006).

[6] J. Aumentado and V. Chandrasekhar, Phys. Rev. B **64**, 054505 (2001).

[7] J. W. A. Robinson, J. D. S. Witt, and M. G. Blamire, Science **329**, 59 (2010).

[8] T. S. Khaire, M. A. Khasawneh, W. P. Pratt, Jr., and N. O. Birge, Phys. Rev. Lett. **104**, 137002 (2010).

[9] C. Klose, T. S. Khaire, Y. Wang, W. P. Pratt, Jr., N. O. Birge, B. J. McMorran, T. P. Ginley, J. A. Borchers, B. J. Kirby, B. B. Maranville, and J. Unguris, Phys. Rev. Lett. **108**, 127002 (2012).

[10] G. B. Halasz, J. W. A. Robinson, J. F. Annett, and M. G. Blamire, Phys. Rev. B **79**, 224505 (2009).

[11] N. Satchell and N. O. Birge, Phys. Rev. B **97**, 214509 (2018).

[12] J. A. Glick, V. Aguilar, A. B. Gougam, B. M. Niedzielski, E. C. Gingrich, R. Loloee, W. P. Pratt, and N. O. Birge, Sci. Adv. **4**, eaat9457 (2018).

[13] S. Voltan, A. Singh, and J. Aarts, Phys. Rev. B **94**, 054503 (2016).

[14] Y. Wang, S. Yang, P. K. Sivakumar, B. R. Ortiz, S. M. L. Teicher, H. Wu, A. K. Srivastava, C. Garg, D. Liu, S. S. P. Parkin *et al.*, arXiv:2012.05898.

[15] J. Wang, M. Singh, M. Tian, N. Kumar, B. Liu, C. Shi, J. K. Jain, N. Samarth, T. E. Mallouk, and M. H. W. Chan, Nat. Phys. **6**, 389 (2010).

[16] F. S. Bergeret, A. F. Volkov, and K. B. Efetov, Phys. Rev. B **68**, 064513 (2003).

[17] S. Takei and V. Galitski, Phys. Rev. B **86**, 054521 (2012).

[18] A. F. Volkov and K. B. Efetov, Phys. Rev. B **81**, 144522 (2010).

[19] M. Kompaniiets, O. V. Dobrovolskiy, C. Neetzel, F. Porrati, J. Brötz, W. Ensinger, and M. Huth, Appl. Phys. Lett. **104**, 052603 (2014).

[20] Y. Pauleau, S. Kukielka, W. Gulbinski, L. Ortega, and S. N. Dub, J. Phys. D: Appl. Phys. **39**, 2803 (2006).

[21] A. K. Singh, U. Kar, M. D. Redell, T.-C. Wu, W.-H. Peng, B. Das, S. Kumar, W.-C. Lee, and W.-L. Lee, npj Quantum Mater. **5**, 45 (2020).

[22] N. Gál, V. Štrbík, Š. Gaži, Š. Chromik, and M. Talacko, J. Supercond. Novel Magn. **32**, 213 (2019).

[23] P. A. Lee and T. V. Ramakrishnan, Rev. Mod. Phys. **57**, 287 (1985).

[24] H. Yamazaki, N. Shannon, and H. Takagi, arXiv:1602.05790 .

[25] J. Wang, C. Shi, M. Tian, Q. Zhang, N. Kumar, J. K. Jain, T. E. Mallouk, and M. H. W. Chan, Phys. Rev. Lett. **102**, 247003 (2009).

[26] O. V. Skryabina, S. N. Kozlov, S. V. Egorov, A. A. Klimenko, V. V. Ryazanov, S. V. Bakurskiy, M. Yu. Kupriyanov, N. V. Klenov, I. I. Soloviev, A. A. Golubov *et al.*, Sci. Rep. **9**, 14470 (2019).

[27] S. Kezilebieke, M. N. Huda, P. Dreher, I. Manninen, Y. Zhou, J. Sainio, R. Mansell, M. M. Ugeda, S. van Dijken, H.-P. Komsa *et al.*, Commun. Phys. **3**, 116 (2020).

[28] G. Chen, S. T. Howard, A. B. Maghirang III, K. Nguyen Cong, R. Angelo, B. Villaos, L.-Y. Feng, K. Cai, S. C. Ganguli, E. Morosan *et al.*, Phys. Rev. B **102**, 115149 (2020).

[29] See Supplemental Material at http://link.aps.org/supplemental/10.1103/PhysRevResearch.4.023133 for further details regarding more transport results of samples 1, 4, 5, 6, 7, and 8, and *M-H* curves of thin-film samples.

[30] Q. Zhang, K. Zhang, D. Xu, G. Yang, H. Huang, F. Nie, C. Liu, and S. Yang, Prog. Mater. Sci. **60**, 208 (2014).

[31] K. Karthik, N. V. Jaya, M. Kanagaraj, and S. Arumugam, Solid State Commun. **151**, 564 (2011).

[32] D. Gao, J. Zhang, J. Zhu, J. Qi, Z. Zhang, W. Sui, H. Shi, and D. Xue, Nanoscale Res. Lett. **5**, 769 (2010).

[33] D. Gao, G. Yang, J. Li, J. Zhang, J. Zhang, and D. Xue, J. Phys. Chem. C **114**, 18347 (2010).

[34] A. Punnoose, H. Magnone, M. S. Seehra, and J. Bonevich, Phys. Rev. B **64**, 174420 (2001).

[35] H. Qin, Z. Zhang, X. Liu, Y. Zhang, and J. Hu, J. Magn. Magn. Mater. **322**, 1994 (2010).

[36] L. Néel, C. R. Acad. Sci **252**, 4075 (1961).

[37] J. Richardson, D. Yiagas, B. Turk, K. Forster, and M. Twigg, J. Appl. Phys. **70**, 6977 (1991).